Remote Sensing of Environment 140 (2014) 652–664

Contents lists available at ScienceDirect

Remote Sensing of Environment

journal homepage: www.elsevier.com/locate/rse

The use of radar satellite data from multiple incidence angles improves surface water mapping

Damien O'Grady [a,*], Marc Leblanc [a,b], Adrian Bass [a]

[a] Centre for Tropical Water and Aquatic Ecosystem Research, 4 James Cook University, MacGregor Road, Smithfield, QLD 4878, Australia
[b] ANR Chair of Excellence, IRD UMR G-EAU, IRSTEA, 34000 Montpellier, France

ARTICLE INFO

Article history:
Received 8 June 2013
Received in revised form 3 September 2013
Accepted 3 October 2013
Available online 26 October 2013

Keywords:
Classification
Flood mapping
Surface water
Radar
ASAR
Incidence angle
Bragg resonance
Wind effects
Absorption
Regression
Aral Sea
Kazakhstan
Uzbekistan

ABSTRACT

Satellite radar data has been employed extensively to monitor flood extents, where cloud cover often prohibits the use of satellite sensors operating at other wavelengths. Where total inundation occurs, a low backscatter return is expected due to the specular reflection of the radar signal on the water surface. However, wind-induced waves can cause a roughening of the water surface which results in a high return signal. Additionally, in arid regions, very dry sand absorbs microwave energy, resulting in low backscatter returns. Where such conditions occur adjacent to open water, this can make the separation of water and land problematic using radar. In the past, we have shown how this latter problem can be mitigated, by making use of the difference in the relationship between the incidence angle of the radar signal, and backscatter, over land and water. The mitigation of wind-induced effects, however, remains elusive. In this paper, we examine how the variability in radar backscatter with incidence angle may be used to differentiate water from land overcoming, to a large extent, both of the above problems.

We carry out regression over multiple sets of time series data, determined by a moving window encompassing consecutively-acquired Envisat ASAR Global Monitoring Mode data, to derive three surfaces for each data set: the slope β of a linear model fitting backscatter against local incidence angle; the backscatter normalised to 30° using the linear model coefficients (σ^0_{30}), and the ratio of the standard deviations of backscatter and local incidence angle over the window sample (SDR). The results are new time series data sets which are characterised by the moving window sample size.

A comparison of the three metrics shows SDR to provide the most robust means to segregate land from water by thresholding. From this resultant data set, using a single step water–land classification employing a simple (and consistent) threshold applied to SDR values, we produced monthly maps of total inundation of the variable south-western basin of the Aral Sea through 2011, with an average pixel accuracy of 94% (kappa = 0.75) when checked against MODIS-derived reference maps.

1. Introduction

1.1. Mapping water using radar remote sensing

The mapping of water extents plays an important role across several fields. In recent years, much attention has been paid to the monitoring of wetland ecosystems, in which inundation patterns are formative in the study of biodiversity and greenhouse gas emissions (Aires, Papa, & Prigent, 2013; Bass et al., 2013; Bwangoy, Hansen, Roy, Grandi, & Justice, 2010; Dronova, Gong, & Wang, 2011; Haas, Bartholomé, Lambin, & Vanacker, 2011). Much research has turned to the use of radar remote sensing to map inundation (Arnesen et al., 2013; Frappart, Seyler, Martinez, León, & Cazenave, 2005; Gan, Zunic, Kuo, & Strobl, 2012; Hostache et al., 2009; Mason, Davenport, Neal, Schumann, & Bates, 2012; Schumann, Di Baldassarre, & Bates, 2009). Radar has several advantages over visual-infra red (VIR) data — being an active sensor system, it can acquire data independently from the position of the sun. Perhaps most importantly, radar can penetrate the cloud cover that prohibits, to varying degrees, the use of VIR data for continuous flood monitoring, or for timely production of flood maps for disaster response purposes. To take full advantage of radar data, much research has been concerned with the task of overcoming some difficulties in the interpretation of radar images. Flat, open water acts as a specular reflector of radar energy away from the sensor. For this reason, water under certain conditions is characterised by a low backscatter return. However, where structures such as vegetation, steep land forms and man-made features emerge through the surface of the water, multiple interactions between such structures and the surface of the water cause "double bounce" effects, which result in a very high return signal. Depending on the relative scale and density of these features with the pixel size of the data image, the result is either a mixed pixel mid-value aggregate of low and high backscatter returns, being hard to distinguish from dry land, or a very high backscatter value,

* Corresponding author.
E-mail address: damien.ogrady@my.jcu.edu.au (D. O'Grady).

0034-4257/$ – see front matter © 2013 Elsevier Inc. All rights reserved.
http://dx.doi.org/10.1016/j.rse.2013.10.006

which in turn can be very hard to distinguish from wet soil or vegetation. Consequently, some research has focussed on overcoming these effects, in terms of the optimal radar configuration (band, polarisation orientation, incidence angle, resolution, time series and data synergy) (Grings et al., 2009; Henderson & Lewis, 2008; Hess & Melack, 2003; Hess, Melack, Filoso, & Wang, 1995; Marti-Cardona, Lopez-Martinez, Dolz-Ripolles, & Bladè-Castellet, 2010; Martinez & Letoan, 2007; Quegan, Le Toan, Yu, Ribbes, & Floury, 2000; Ribbes, 1999). Another common problem with the identification of open water with radar data is caused by the waves induced on the surface of the water by winds over a particular speed. The phenomenon is the result of the roughened water surface reducing the proportion of energy reflected away from the sensor.

Research has identified the particular wind speeds and relative orientations that cause this effect, and the best radar configurations that may be used to minimise it (Liebe, van de Giesen, Andreini, Steenhuis, & Walter, 2009). However, the problem does persist, and in certain regions, can narrow the opportunity for water classification using radar data to an almost unusable level, as will be seen.

1.2. The use of multiple incidence angle, low spatial–high temporal-resolution radar data

Backscatter values over multitemporal time series of satellite radar data have been used as a tool to detect land use, by analysis of the variation of backscatter with respect to time, and to changes in, for example, plant phenology and biomass. Le Toan et al. (1997) model the interaction of C-band radar with rice and water at various stages of crop development, in order to monitor rice farming on a large spatial scale. Their research is extended by Ribbes (1999), who analyse observed backscatter values from RADARSAT against rice height, biomass and age, for the same purpose. Quegan et al. (2000) recognised the potential of using the relatively low temporal variability of backscatter values in forest compared with other land cover types as a forest segregation technique. Martinez and Letoan (2007) incorporated the temporal variation of L-band JERS-1 data into their classification technique when mapping flood patterns and vegetation in the Amazon floodplain. Their time series is used to increase the effective number of looks in the calculation of a mean backscatter coefficient, which is coupled with a temporal change estimate, derived over the time series, to classify flood conditions as *never*, *occasionally* and *always flooded*, together with broad vegetation types. Specific analysis of the comparative response of C-band radar to water at low and high incidence angles was made by Töyrä et al. (2001), who advise that at high incidence angles, wave-induced effects are overcome, and that at low angles, the return signal from water has similar values to those for dry land. For our purposes, it is this very quality that offers a potential means for better classification of water. The diffuse reflections from dry land at low incidence angles are not expected to reduce significantly at higher angles, and the low backscatter values returned from dry sand are not expected to increase significantly at lower angles, thus distinguishing both surface conditions from water. For this reason, a time series of radar data acquired at multiple incidence angles is desirable.

Some research has focussed on the advantages of the high temporal frequency of the systematically-acquired C-band radar data from the European Space Agency's (ESA) Advanced Synthetic Aperture Radar (ASAR) on the Envisat satellite, operating from March 2002 until April 2012, when full operation of the satellite was lost (Baup et al., 2007; Mladenova et al., 2010; O'Grady, Leblanc, & Gillieson, 2011; O'Grady, Leblanc, & Gillieson, 2013; Park et al., 2011). In ASAR's Global Monitoring (GM) mode, the sensor systematically acquired data at times when the other modes were not required, providing high repeat coverage ($\approx 0-4$ times per week) across much of the globe (O'Grady et al., 2011). The data covered the full orbit width across the whole swath of incidence angles (14–44°), with a pixel size of 500 m and a nominal spatial resolution of 1 km. Such a coarse spatial resolution obviously limits the scale of use to which GM data may be put. One application, as was originally envisaged by ESA, is the monitoring of sea ice (Zink et al., 2001). Others have drawn much information on

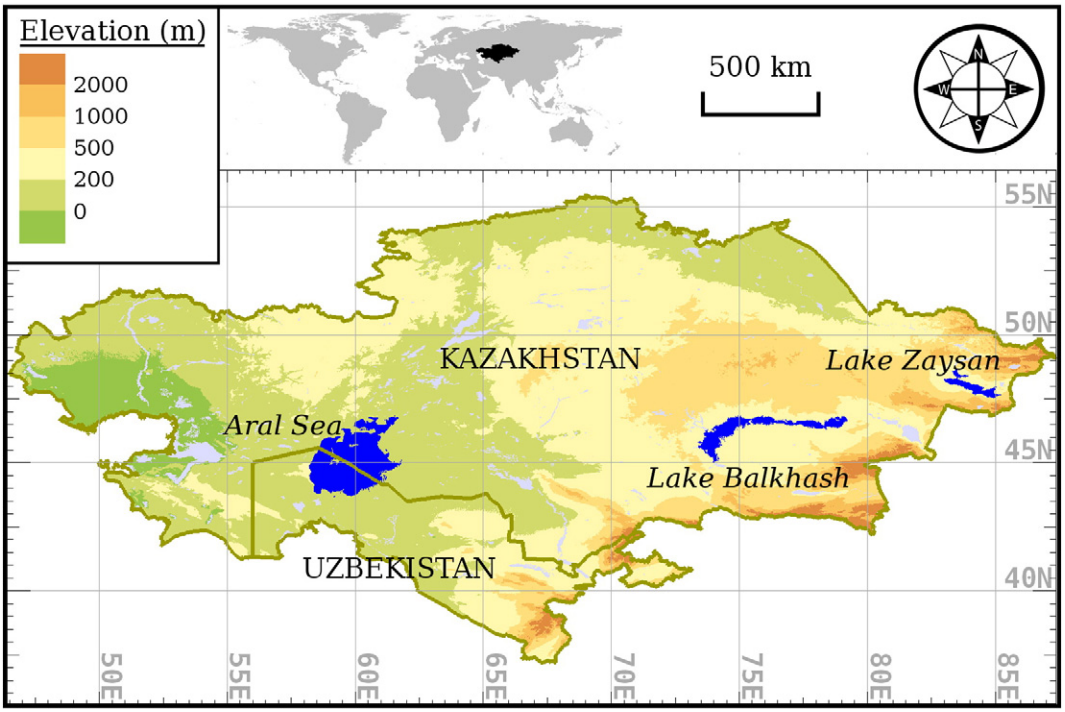

Fig. 1. Map of regions under study: the Aral Sea in Kazakhstan/Uzbekistan, and Lakes Balkhash and Zaysan in Kazakhstan. Map produced from an SRTM90 DEM downloaded from the Consortium for Spatial Information (Jarvis et al., 2008).

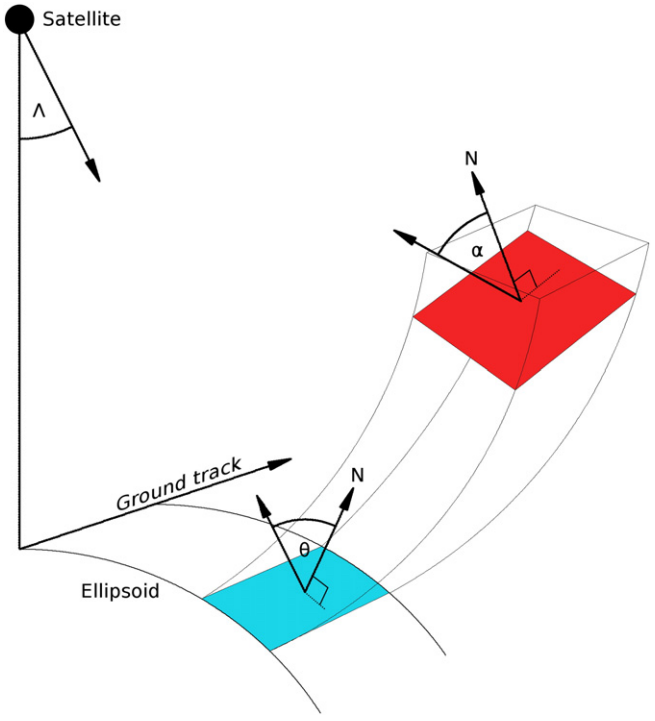

Fig. 2. Incidence angle θ, look angle Λ and local incidence angle, α. The blue polygon represents the position of the target pixel with respect to the ellipsoid model, which is calculated geometrically from the return-time of the radar signal, along with the incidence angle θ. The red polygon represents the true position and orientation of the target, at a particular height above the ellipsoid, and with actual (*local*) incidence angle α. The terrain displacement and α may be calculated using a Digital Elevation Model and satellite configuration data.

soil moisture from GM data, producing a systematically generated soil moisture product (Bartsch et al., 2009; Mladenova et al., 2010; Pathe, Wagner, Sabel, Doubkova, & Basara, 2009).

In past work, we have shown the value of GM data in the mapping of large-scale flooding, such as the 2010 Indus floods in Pakistan (O'Grady et al., 2011), and the inundation of the Flinders floodplain in Australia in 2009 (O'Grady & Leblanc, 2013). In the case of the flooding in Pakistan, it was observed that absorption of the radar signal in very dry sand, adjacent to the flooding, can add further complexity to the segregation of land and water. This problem was mitigated to some extent by image differencing techniques. Subsequently to this, we showed that the rate of change of backscatter with respect to incidence angle was sufficiently different between water and land, to be able to distinguish the two, independently of absorption in dry sand. The technique employed was to carry out pixel-wise regression, modelling radar backscatter against incidence angle across a time series for a given period, according to the model

$$\sigma^0_\alpha = \beta \cdot \alpha + A \tag{1}$$

where σ^0_α is the backscatter, in decibels, at local incidence angle α, β is the slope and A is the intercept at $\alpha = 0$.

The slope of the model, β, over water, was found to be approximately double that over land. The separability between water and land using β was seen to be far greater than that using backscatter alone. The influence of wind-induced water surface roughening on the outcome was one of chance coincidence between the incidence angles and the timing of wave-inducing winds.

1.3. Research questions

There are several questions that remain to be explored in the relationship between radar backscatter and incidence angle, for the mapping of water extents. The regression methods described above depend upon the temporal frequency of data coverage to determine the temporal resolution and quality of land–water classification output. The extent of this needs to be established, and this should enable us to predict the potential use of such methods with new sensors on anticipated satellite missions. The quantity of data available affords us the ability to carry out multiple regression calculations on a large data set in several different regions, to establish the relative stability of thresholds using backscatter and β, providing a further measure of the potential value of such methods in the future.

We targeted three lakes in Central Asia: The Aral Sea in Kazakhstan/Uzbekistan, and Lakes Balkhash and Zaysan, both in Kazakhstan (see Fig. 1). Each of the lakes is surrounded by land which demonstrates absorption of GM radar energy, and each demonstrates the significant presence of wind-induced roughening. The three lakes also have a reasonable east–west (cross-orbit) spatial range, increasing the number of orbit paths from which data may be drawn, thus ensuring good availability of data acquired at the full range of incidence angles. The Aral Sea region was given closer consideration, due to the variability

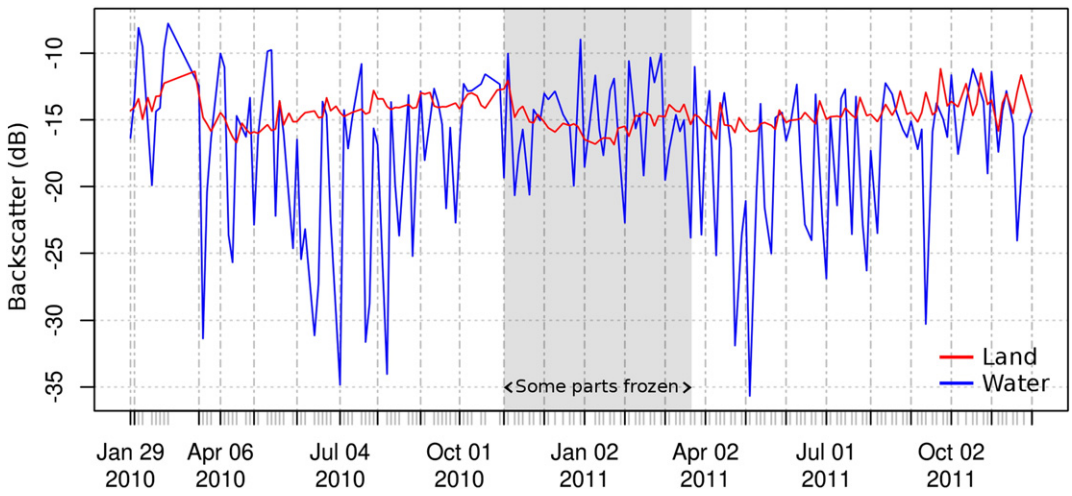

Fig. 3. Median backscatter values throughout the Aral Sea time series for land (red) and water (blue). The relatively higher values for water in the mid-winter months are due to ice. However, we know from MODIS imagery that the sea was not frozen through October 2010. The high median values through September and October are attributed to wind effects on the water surface. The data between November and April (inclusive) were excluded from the separability analysis to avoid ice.

Table 1
Bodies of water chosen for this study, and the bounds of their associated study regions.

Name	Country	South latitude	North latitude	West longitude	East longitude
Aral Sea	Kazakhstan/Uzbekistan	44°11′05″ N	46°53′07″ N	058°05′37″ E	062°27′44″ E
Lake Zaysan	Kazakhstan	47°30′23″ N	48°44′42″ N	082°54′26″ E	085°18′27″ E
Lake Balkhask	Kazakhstan	44°38′15″ N	47°03′27″ N	072°59′18″ E	079°25′37″ E

of its extents (Breckle, Wucherer, Dimeyeva, & Ogar, 2012). We had previously acquired GM data between September 2009 and December 2011. Given the potential presence of ice on the lakes between November and April, these months were excluded from our regression calculations. The resulting data set comprised 393 GM files.

2. Method

Radar backscatter returned to a satellite sensor is a function of, among other things, the angle of orientation of the target surface with respect to the satellite sensor, known as the *local incidence angle*, α (see Fig. 2).

When using image data acquired over a wide swath, the returned signal corresponds to varying incidence angle (θ), due to the differing *Look angle*, Λ, and to the curvature of the ellipsoid. However, the actual orientation and height of the target result in the *local* incidence angle, α, influencing the scattering behaviour of the radar signal. The relationship between the backscatter (σ^0, usually converted to decibels) and α for a given image pixel varies with the surface conditions (for example ground cover and surface roughness) and with some average of the orientation of the surfaces within the pixel area, in relation to the sensor. Where an entire pixel represents surface water the orientation is practically uniform, and the surface conditions, in the absence of radar-visible waves, homogeneous. Due to the fact that the water surface acts as a specular reflector of microwave signals, the rate of reduction of σ^0 with respect to α is higher for water than for other surfaces. This has allowed us to successfully map the extents of a water body, using a time series of radar data at multiple incidence angles, to a much higher degree of accuracy than was possible with a single radar image (O'Grady et al., 2013). The process allows the complete distinction between water and land, including dry sand. Certain wind conditions do disturb the water surface, returning a very high signal instead of the low value associated with specular reflection away from the sensor, which we expect from smooth water. For this reason, the success of the regression model on a small time series frequency (n) is unpredictable, with the sign and magnitude of β depending on the timing of the adverse wind conditions within the time series. One way to attempt to overcome this problem is to ignore the sign of β, and base a classifier decision on the absolute slope magnitude. In this research, we accept the possible presence of wind effects as simply a further contributor to distinctly higher variability of backscatter from water compared with land, and we measure this by calculating the ratio of standard deviations (SDR) of the backscatter σ^0 and α at each pixel through the time series, such that

$$\mathrm{SDR} = \frac{\mathrm{sd}\left(\sigma^0\right)}{\mathrm{sd}(\alpha)} \tag{2}$$

where sd is the standard deviation of values of a pixel across the time series.

The denominator in Eq. (2) is essential, as values of σ^0 at different pixels across a time series may arise from different data frequencies with quite different ranges of local incidence angle, depending on the proximity of the pixel in relation to the various orbit tracks from which the data was acquired. We would expect a much higher SDR for water than for land. For the Aral Sea region, this is demonstrated in Fig. 3, which plots median backscatter values of water and land throughout the data set. However, it remains to be seen whether this measure is an improvement over β or σ^0 for automating the classification of surface water.

Research in the field of radar remote sensing generally regards incidence angle as a property which must be observed and optimised for purpose (e.g. Grings et al. (2009), Lang, Townsend, and Kasischke (2008)), or that must be corrected for (e.g. Menges, Van Zyl, Hill, and

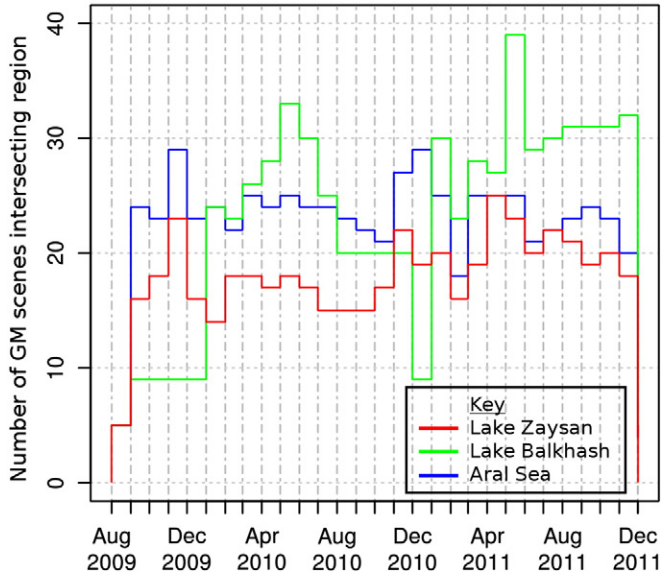

Fig. 4. The number of available GM data images intersecting the study regions per month, between August 2009 and December 2011.

Table 2
MODIS daily surface reflectance data used for this paper (USGS, 2013).

Terra/Aqua	Date	Tile	
		H	V
T	2010–01–07	22	04
T	2010–01–18	22	04
T	2010–03–23	22	04
T	2010–04–01	23	04
T	2010–07–01	23	04
T	2010–07–02	22	04
T	2010–07–05	22	04
T	2011–01–07	22	04
T	2011–07–02	22	04
T	2011–07–05	23	04
T	2012–01–18	22	04
A	2010–05–18	22	04
A	2010–11–08	22	04
A	2011–03–17	22	04
A	2011–04–16	22	04
A	2011–05–17	22	04
A	2011–06–16	22	04
A	2011–07–16	22	04
A	2011–08–15	22	04
A	2011–09–15	22	04
A	2011–10–16	22	04
A	2011–11–09	22	04

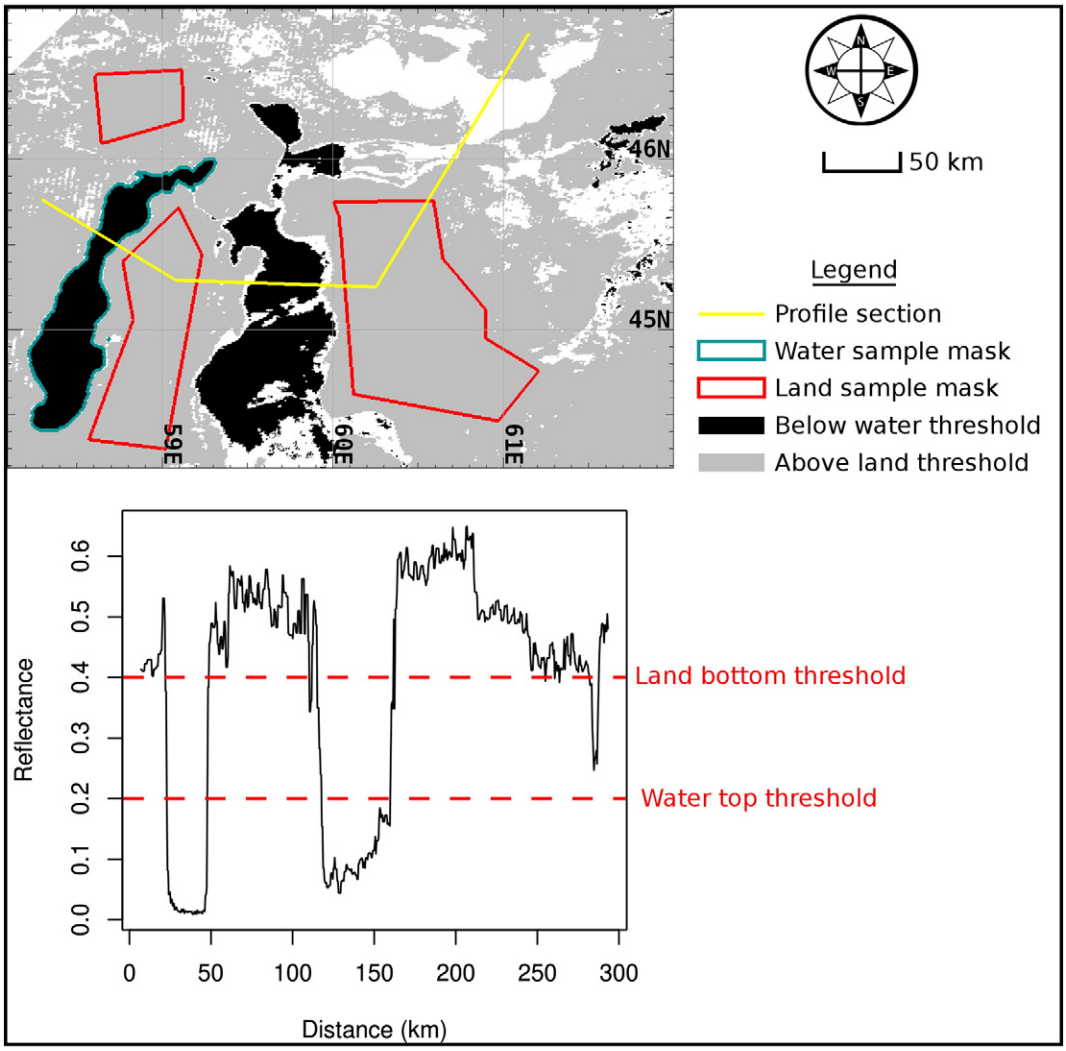

Fig. 5. (Top) Map showing transect and sample regions at the Aral Sea region of interest. The yellow line on the map shows the transect from which the values of the MAXIMUM MODIS SWIR were extracted for the profile plotted below. Rather than using a single land–water threshold, two "safe" thresholds were drawn from the profile plot, allowing a buffer for uncertain boundary conditions, and enabling a high degree of certainty for the classification of permanent land (shown on the upper map in grey) and water (shown as black). From these, contiguous subregions were chosen for sampling, shown as green and red outlines.

Ahmad (2001)). Here we seek to draw the benefits of the use of multiple incidence angles by observation of the difference in response between water and land at different angles of incidence.

2.1. Data acquisition and pre-processing

Regions of interest were defined for the three lake environs as shown in Table 1.

Envisat ASAR Global Monitoring Mode (GM) data were downloaded systematically from ESA's *Earthnet Online* Portal through a Category 1 Fast Registration agreement (ESA, 2009). All available files intersecting the study regions between August 2009 and December 2011 were processed (see Fig. 4 for quantities). The *Next Esa Sar Toolbox* (NEST) was used to pre-process the data. NEST is open source (GNU GPL[1]) software, developed for ESA and made available via its website (NEST, 2013). The Range-Doppler method (Small & Schubert, 2008) was used to orthorectify the data with the SRTM 90 m void-filled Digital Elevation Model (DEM) downloaded from the Consortium for Spatial Information website (Jarvis, Reuter, Nelson, & Guevara, 2008). Radiometric normalisation was applied (Kellndorfer, Pierce, Dobson, Member, & Ulaby, 1998), and the backscatter (σ^0) and local incidence angle (α) values were extracted as two image bands, masked to the regions of interest.

Moderate Resolution Imaging Spectroradiometer (MODIS) imagery was downloaded from the U.S. Geological Survey's GLOVIS website (USGS, 2013). Aqua or Terra 500 m daily surface reflectance products MYD09GA or MOD09GA were selected as appropriate to minimise cloud cover. These are listed in Table 2.

2.2. Regression procedure

Our task was to determine the relative separability of land and water using β and SDR, and to compare the results with what could be achieved with standard backscatter values. To do this, groups of consecutive data images were used to perform regression at various temporal scales. Each regression resulted in three image files for the region, from which statistics could be sampled from known water and land regions, in order to determine the separability between them. In the case of backscatter, we know this to be dependent on local incidence angle. For this reason, the vales were normalised to a local incidence angle of 30° prior to averaging over the group, giving us σ^0_{30}. The β

[1] http://www.gnu.org/copyleft/gpl.html

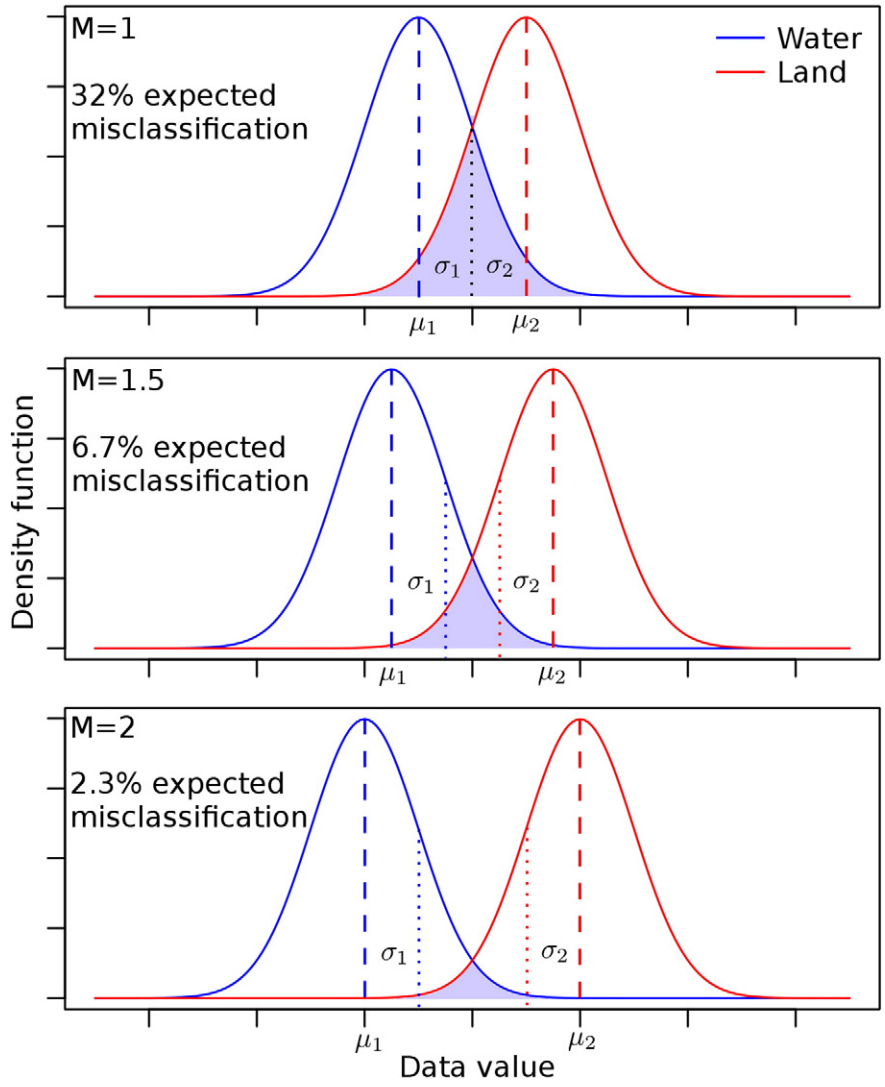

Fig. 6. The schematic density plots above demonstrate the consequences of separability (M) values of 1, 1.5 and 2 on resultant land-water classifications performed using thresholds on the data value. The model is simplified, but it gives a general idea of the meaning of M. The results assume an equal number of pixels of land and water, and that the distribution of data values for each follows a normal distribution. Assuming the chosen threshold in each plot was at the central data value, the shaded area beneath the plots represents the misclassified pixels. The percentage of pixels misclassified where separability equals 1, 1.5 and 2 would then be 32%, 6.7% and 2.3% respectively.

value used to do this was taken from the regression carried out over the entire time series. The procedure was split into three parts:

1) Determining the relative land–water separability using σ^0_{30}, β and SDR;
2) Analysis of optimum thresholds for each value; and
3) The creation of a monthly time series of water extents for the Aral Sea through 2011.

For each location, MODIS images were reprojected and masked to the region of interest. In order to establish sample regions of permanent water, an image was computed as the maximum of MODIS Band 6 (SWIR) values across the full MODIS data set. A section through the lakes was taken, and the profile of maximum SWIR values was plotted and analysed (see Fig. 5). Conservative thresholds were established for water and land, allowing room for uncertainty in the values between the thresholds. From the resulting binary land–water image, core polygons were created which were to form the regions from which water and land pixel values were sampled throughout the analysis.

For the separability analysis, regression was carried out on individual groups within time series, where group size (number of images) = 2,4,8,16,32…N where N = total number of images for the region of interest.

2.3. Relative separability analysis

The establishment of a value of β, by which to determine the presence of water, requires a regression calculation. The integrity of the result depends on the number of images contained within the time series on which it is based. Radar data is quite noisy, and sufficient backscatter values must be acquired over a broad enough range of incidence angles to obtain a good model fit. We set out to determine the number of consecutive data acquisitions required for segregation methods using β and SDR to produce robust results. This, in turn, would allow us to relate temporal frequency of radar data coverage to the temporal precision by which we may be able to use this method to monitor surface water extents.

To compare separability, the M-statistic has been used by others (e.g. O'Grady et al. (2013), Smith et al. (2007), Lasaponara (2006), Veraverbeke, Harris, and Hook (2011)), which is calculated as $|\mu_1 - \mu_2|/(\sigma_1 + \sigma_2)$, where μ_1 and μ_2 are the means and σ_1 and σ_2 are the standard deviations of values for the two categories being

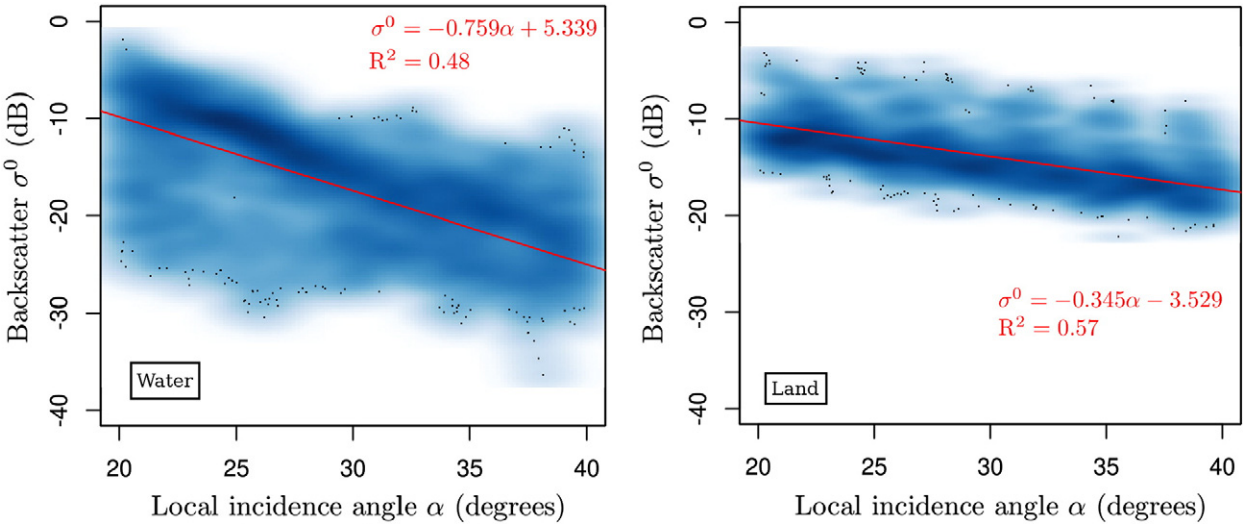

Fig. 7. Scatter plot of radar backscatter values σ^0 against local incidence angle α for all pixels sampled from permanent water (left) and permanent land (right), throughout the entire time series. This involved 2,285,832 data pairs for water and 8,647,965 data pairs for land. The red lines show the linear fit, with slopes and intercepts as shown inset.

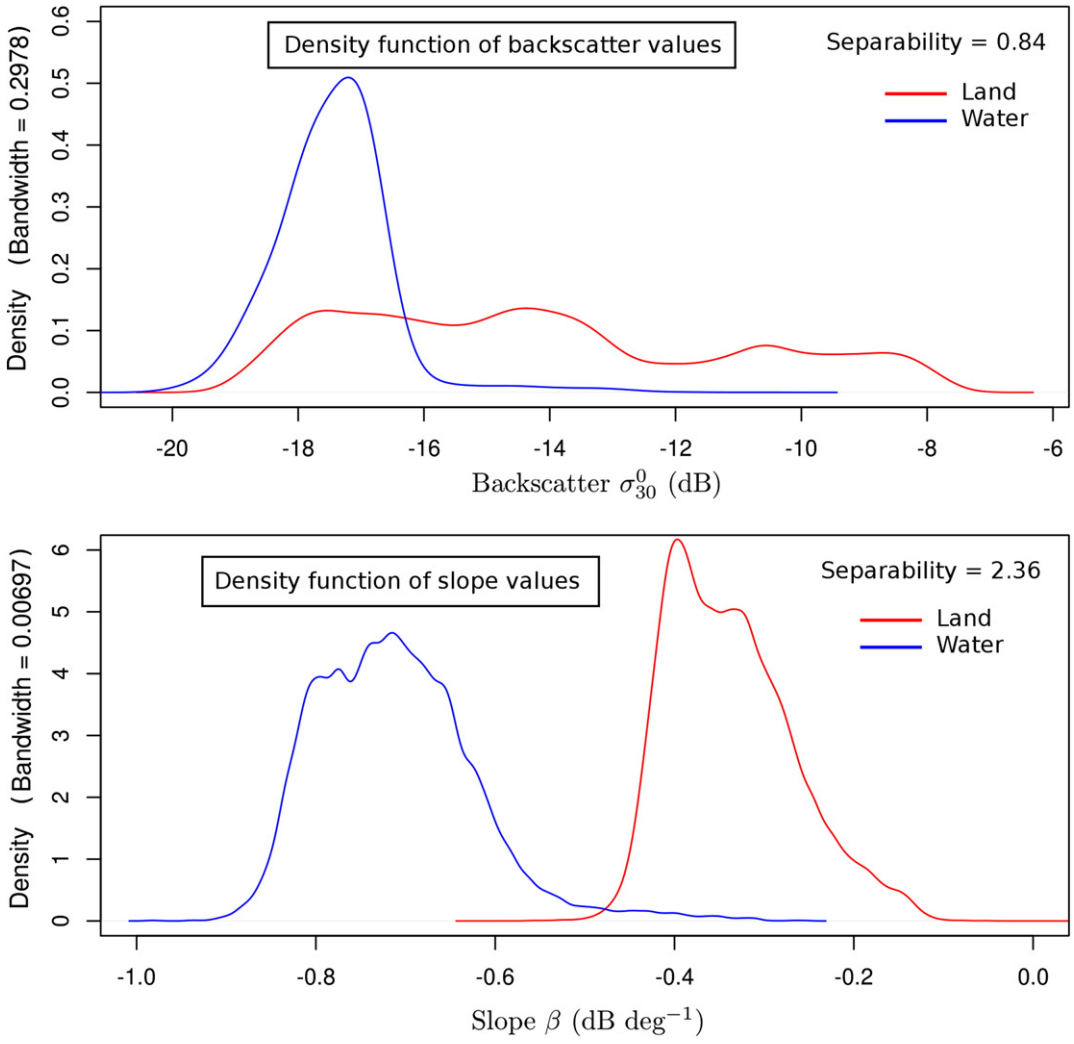

Fig. 8. Probability density functions showing the distribution of normalised backscatter values (top) and slope values (bottom), for pixels representing permanent land (red) and permanent water (blue) at the Aral Sea study region. Slope values were taken from the full regression carried out over the whole time series for the Aral Sea region of interest. The final slope values for each individual pixel were then used to normalise the backscatter values in the individual images to 30°. The separability indices (M-statistic) between land and water were 0.84 and 2.36 for backscatter and slope, respectively.

compared. The M-statistic gives a measure of the separability of values associated with separate means, in terms of their combined standard deviation. This is explained graphically in Fig. 6.

2.4. Threshold analysis

In order to gauge the stability of thresholds for each of σ^0_{30}, β and SDR, the data for each study region was arranged into groups, each with 14 (or less) consecutive images. For each group, regression was carried out to establish maps for σ^0_{30}, β and SDR. For each of these, an optimised threshold was calculated and recorded. To achieve this, all pixel values for each of permanent land and permanent water were extracted. Starting with a threshold value t half way between the mean values for land and water, the number of cells that would be erroneously classified using a threshold of t was calculated. The optimum threshold was then found by raising and lowering t and repeating the process through binary tree iteration until the resultant value converged to three decimal places. In this way, 20 optimised threshold values for each of σ^0_{30}, β and SDR were established for comparison.

To measure the accuracy corresponding to the established thresholds, binary reference water–land maps were created for each of the months March through to November 2011, using a 15% reflectance threshold on MODIS Band 6 (SWIR) images acquired mid-way through each of the corresponding months. Similar binary maps were then produced using σ^0_{30} and SDR, by applying the median thresholds established above for each. Accuracy of classification for each month using σ^0_{30} and SDR was then gauged from contingency tables by calculating Cowen's Kappa statistic for each (Hudson & Ramm, 1987).

2.5. Mapping of monthly maps of Aral Sea extents

Having established SDR as the measurable whose values were most easily segregated between land and water, the task of producing a time series of lake extent maps was undertaken for the Aral Sea. For this purpose, a series of multiple aggregations was carried out, one for every data image in the entire set (less 10), using a rolling stack of the five preceding and four succeeding image files, ensuring that there were always ten image files involved in each aggregation. Each aggregation simply involved calculation of the standard deviations of σ^0 and α through the stack for each pixel, in order that the SDR could be computed and a map created. Once the full set of SDR maps was complete, the pixel-wise SDR maxima were calculated for each calendar month. The reason that the maximum was chosen, rather than the mean or the median, was the decision to reflect, in the final product, whether or not water had been detected in a pixel at any time during that month, and also to mitigate any wind-induced effects. Next, the SDR threshold of 0.349 dB deg^{-1}, determined in the threshold analysis described above, was applied to the monthly SDR images. Finally, a 3×3 modal neighbourhood filter was applied in order to remove most of the edge effects found at the extremities of the orbit tracks, to produce monthly water maps.

3. Results & discussion

3.1. The use of backscatter variability to classify open water

Martinez and Letoan (2007) are able to classify regions according to flood dynamics and vegetation classes, as a function of their mean backscatter coefficient and their temporal variability, which is attributed to soil moisture, vegetation state and flood progress. In our case, we take a moving window of time series data to represent a snapshot in time. Regression is used to derive a mean backscatter coefficient and two measures of the variability of backscatter, specifically with respect to the corresponding variation of incidence angle. The results are the new time series sets (σ^0_{30}, β and SDR), with which there is a trade-off between temporal resolution and regression correlation. The land–water separability for each parameter surface is matched against each other for multiple window sizes. Martinez and Letoan (2007) use L-band JERS-1 data, which is less susceptible to wind-induced effects on open water that cause the deviation from the low backscatter values following specular reflection. In our case, we wish to use multiple time series windows to produce pseudo-instantaneous snapshots of water extents, and for this we have capitalised on the availability of GM data. Being in the C-band spectral range, GM data is far more susceptible to such wind effects, which therefore play an important part in the classification results for the three result sets.

3.2. Distribution of backscatter values on water and land

Despite the comparative variability of land and water backscatter values, the inter- and intra-location slope values resulting from the

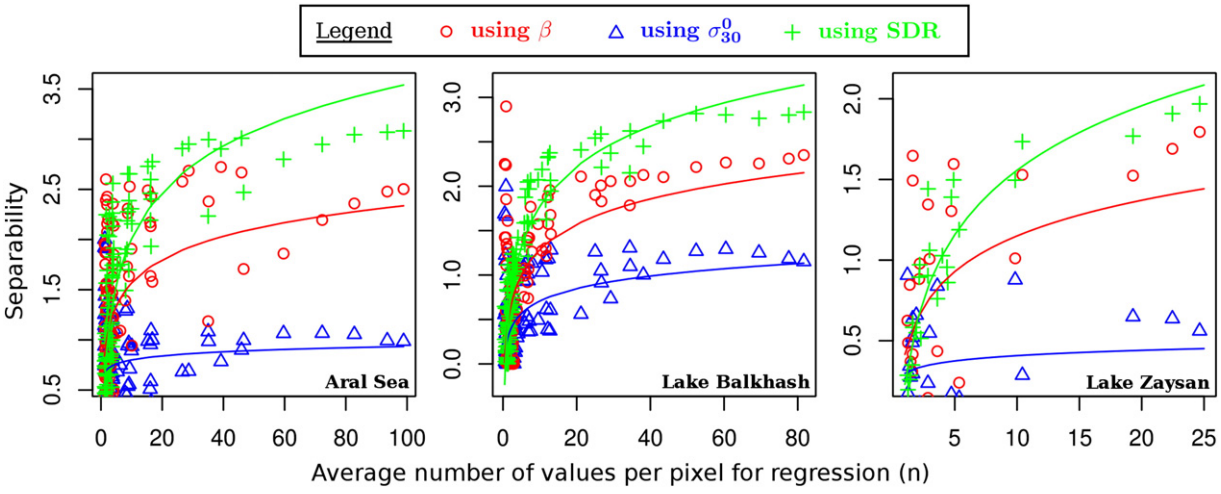

Fig. 9. Separability index (M-statistic) between land pixels and water pixels in the three study regions, against the number of data instances involved in the linear regression calculations (n). Comparisons are made in separability using the mean normalised backscatter values (σ^0_{30}, shown as blue triangles), the slope values (β, shown as red circles) and the Standard Deviation Ratios (SDR, shown as green crosses). To the left of the plots, where few data values were used to carry out the regression, separability varies widely. The superiority in separation using SDR becomes quite clear above around $n = 5$, where very high separability is achieved using β and SDR, although the range of success is large. This range contracts after about $n = 10$.

linear regressions proved to be consistent for water, with a mean value of $\beta = -0.756$ and a standard deviation of 0.013. For land, β had a mean of -0.281 and a standard deviation of 0.065. Scatter plots representing the whole Aral Sea data set are shown in Fig. 7, along with their linear model coefficients. The variability of the absolute water backscatter values is reflected in the R^2 value of 0.48.

3.3. Land–water separability analysis

For the regression over the full sets of data, land–water separability (M-statistic) values using mean σ^0_{30} were 1.81, 0.91 and 1.40 for the Aral Sea, Lake Zaysan and Lake Balkhash respectively. Using β, values reached 2.73, 1.79 and 2.35. What this difference means for the Aral Sea region can be seen in the density plots in Fig. 8. These plots show the relative frequency of pixels against corresponding pixel values, independently for water and land. The plot at the top, representing normalised backscatter values, shows that land pixels cover the full range of σ^0_{30} values. Very low values (σ^0_{30} between -19 and -16 dB) were returned from the very dry sand regions of the old lake bed existing mostly between the 1960 and1990 shorelines of the original lake, and the highest values ($\sigma^0_{30} > -9$ dB) were returned from salt flats between the 1990 and present shorelines of the south-eastern basin. The distribution of β values in the lower plot tells a very different story, with the overlap of values (and therefore expected commission–omission error) being less than 2%.

The separability seen in these density plots results from the regression over the whole data set for the Aral Sea. As such, they are not useful in terms of gaining a snapshot of the extents of water at any one time.

In order to observe the relative performance of σ^0_{30}, β and SDR in the potential mapping of surface water extents, the separability between values of permanent water and permanent land was calculated using sets of consecutive image data of various sizes, ranging from three images to the full dataset. The results are shown in Fig. 9. As an individual data image does not often cover an entire sample region spatially, separability is plotted against the average data frequency per

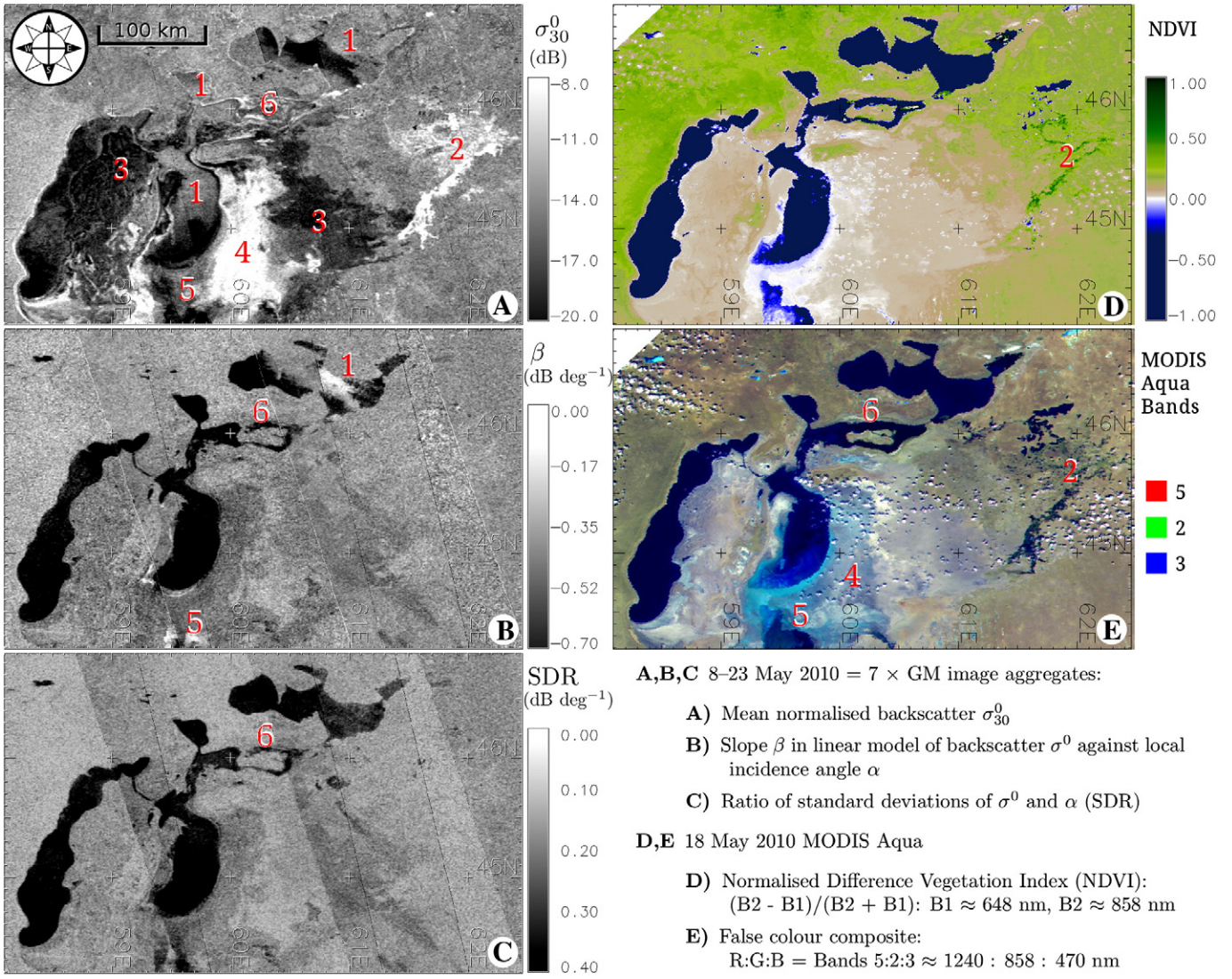

Fig. 10. The Aral Sea between 8 and 23 May 2010, as depicted by GM and MODIS data. Images A, B and C are all produced from the same 7 GM data files: A) Mean σ^0_{30}; B) Slope β; C) SDR. Images D and E are produced from a MODIS Aqua image acquired on 18 May 2010: D) NDVI; E) 5:2:3 Composite. Wind induced roughening effects (1) are present at various locations in the σ^0_{30} image A, but only at one location in the β image B, and are almost absent from the SDR image C. Absorption of the radar signal in dry sand (3) makes the separation of water and land difficult in the σ^0_{30} image A, whilst this effect is not seen in images B and C. The very high (bright) values (4) in image A represent the barren salt flats west of the 1990 eastern coastline (Breckle, Wucherer, & Dimeyeva, 2012a). Similar bright values (2) caused by multiple reflections between vegetation and water at the delta of the Syr Darya river are not seen in either the β image (B) or the SDR image (C).

pixel of the sample area (n). In the case of Lake Zaysan (the right-most plot), having removed from the data set the months between April and November (when the lake freezes), the sample size became quite small, although the trends did follow those of the other two lakes.

3.3.1. Low n values

Where $n \leq 5$, the relative separability between the measured quantities depends greatly on chance outcomes. For β, the presence of wind effects causing high values where incidence angles are large in one image, and the subsequent absence of such effects (causing low returns) where incidence angles are small, will result in a positive regression slope, or a mid-range β value once averaged with more characteristic low values. In such a case, the SDR value remains high, indicating water, as this value reflects high variability irrespective of direction.

This suggests the potential for the two data sets to complement each other in the mapping of surface water. Where $n = 1$, we are limited to the use of σ^0. This can be normalised to a mid-range incidence angle using a prior established β value, but, as we know, β varies by a factor of two, according to whether a particular pixel represents water or land. As it is this distinction we are aiming to make, the merits of carrying out such a correction on a *single* data image are limited.

3.3.2. High n values

Where $n >= 10$, relative land–water separability between the methods is seen to stabilise. At this point, the clear potential to segregate land from water using β or SDR, instead of the mean σ^0_{30} image becomes clear. Beyond $n \approx 20$, separability for SDR remains consistently higher than for β and σ^0_{30}.

3.4. Integrity of resultant water maps

Fig. 10 shows the Aral Sea region in mid May 2010. Inset images A, B and C are all products of the same 7 GM images acquired between 8 and 23 May 2010. Image A values represent the mean normalised backscatter, σ^0_{30}, in decibels. Various effects can be seen here. The expected low (dark) backscatter values in image A are obscured by wind-induced roughening effects in large parts of the North Aral Sea and south-east basins (1). High value (white) backscatter returns at 2 are attributed to the "double-bounce" multiple reflections between vertical components of vegetation and surface water in the wetlands of the Syr Darya river delta. Very low (dark) backscatter returns are observed where the former lake beds comprise sandy desert (3), due to absorption of the radar signal. In contrast, where the former lake bed comprises bare salt flats and swamps (Breckle, Wucherer, & Dimeyeva, 2012), a very high (bright) backscatter response is observed (4). Image B represents the slope β of the regression model. Wind-induced roughening effects are still present in this image (1), though to a much lesser degree than in the σ^0_{30} image. The extent of the effect is not the same, as the orientation (sign) of the slope depends on the timing of the wind conditions with respect to the relative incidence angle values. In the SDR image (C), such wind effects have almost disappeared completely. Locations 5 and 6 show areas where the extent of water that can be discerned in image E appear reduced, due possibly to wind effects or to the mixing of values from sub-pixel heterogeneity.

3.5. Relative performance of β and SDR

Results of the separability analysis described, and of the comparison of resultant images produced using the β and SDR methods as seen in Fig. 10, indicate the superiority of the simpler SDR method over the use of β. This is attributed to the fact that the calculation of β depends upon the adherence of the data to a linear model, and takes no account of the variability of the backscatter values. A single coefficient is calculated, which depends upon the quantity of backscatter values returned by specular reflection from the relatively undisturbed water surface having a greater influence than that returned via diffuse scattering, or following multiple interaction. The former displays a strong relationship with local incidence angle, giving us high separability between water and land using this method, whilst the latter does not.

Given that the SDR method is indiscriminate with regard to the drivers behind the level of variability of a backscatter signal, it is likely that significant differences in surface wetness on land across the sample data of a particular period would produce SDR values similar to those observed over water, although to what extent this might occur has not been tested in this study. In such cases it is feasible to assume that concurrent calculations of β could augment the SDR results and that the two could be used together in a decision-tree analysis to optimise the separation of water and land.

3.6. Comparison of stability of thresholds of β and σ^0

The optimal threshold values of σ^0_{30}, β and SDR by which to demarcate the division between land and water, calculated across multiple data groups in the method described, are tabulated in Table 3. Along with the median values, the robust coefficient of variation C_v (Mean absolute deviation ÷ MEDIAN) is shown as a measure of

Table 3
Thresholds for values of σ^0_{30}, β and SDR, optimised for the separation of surface water from land, based on regression calculations for the three regions combined. n is the mean data frequency per pixel.

n	Threshold		
	σ^0_{30}	β	SDR
11.1	−12.869	−0.607	0.318
11.0	−15.259	−0.512	0.369
10.8	−15.597	−0.596	0.350
9.7	−16.346	−0.400	0.305
10.5	−15.573	−0.627	0.379
10.5	−16.503	−0.548	0.371
10.0	−14.794	−0.712	0.378
7.0	−15.887	−0.574	0.341
8.0	−13.932	−0.625	0.370
8.7	−14.351	−0.516	0.318
7.7	−14.124	−0.604	0.338
8.3	−14.802	−0.633	0.372
7.8	−14.663	−0.508	0.311
7.7	−15.222	−0.553	0.356
8.0	−14.806	−0.551	0.293
6.8	−14.824	−0.638	0.340
3.8	−13.567	−0.727	0.368
7.8	−15.169	−0.502	0.346
12.7	−14.745	−0.651	0.401
12.0	−15.298	−0.443	0.336
Median	−14.815	−0.586	0.349
Units	dB	dB/deg	dB/deg
Robust C_v	−0.047	−0.128	0.095

Table 4
Figures taken from contingency tables of classification accuracy tests done of monthly Aral Sea extent maps using rolling SDR calculations and mean σ^0_{30} values, against MODIS SWIR (Band 6) binary water maps. Fixed thresholds were used throughout for all of the classification and reference maps: MODIS Band 6 reflection values below 15% were matched against SDR values above 0.349 dB deg^{-1} and σ^0_{30} values below −14.815 dB.

Month 2011	σ^0_{30}		SDR	
	% Obs. correct	Kappa stat.	% Obs. correct	Kappa stat.
3	67.44	0.13	86.18	0.60
4	68.55	0.30	94.90	0.82
5	65.57	0.21	95.27	0.80
6	61.65	0.20	94.91	0.79
7	66.83	0.24	96.30	0.83
8	69.09	0.25	96.77	0.84
9	65.78	0.19	95.71	0.79
10	67.07	0.10	93.95	0.72
11	71.10	0.22	95.34	0.73

relative distribution. Of the three measurables, β has by far the greatest C_v, and would seem likely to require a case-by-case sensitivity analysis to establish a threshold depending on the merits of the data set being used. Optimal thresholds for both σ^0_{30} and SDR, on the other hand, demonstrate low C_v values, suggesting the opportunity to be able to apply the median threshold value more broadly in order to achieve the best possible separation of land and water, with a single data value. What remains to be seen is the possible spatial accuracy that can be achieved with each.

The results of the accuracy tests on land–water maps created using the above median thresholds for σ^0_{30} and β are shown in Table 4. The relative percentages of pixels observed correctly are perhaps better reflected by the Kappa statistics, which account for the proportion of pixels belonging to each class in the reference image.

Cowen's kappa statistic has been used extensively in the past as a measure of classification accuracy (Ban, Hu, & Rangel, 2010; Gray & Song, 2013; Hudson & Ramm, 1987; Kellndorfer et al., 1998; Liebe et al., 2009; Martinez & Letoan, 2007; Rignot, Salas, & Skole, 1997; Töyrä & Pietroniro, 2005; Töyrä et al., 2001). In recent years there has been discussion as to whether or not it is a good indicator of accuracy. This discussion centres largely on what information is missing from the single kappa value, and opponents to its use suggest that analysis of the contingency table may be more useful for the analysis of classification performance (Pontius & Millones, 2011). In our case, kappa is useful. For the Aral Sea region, we are looking at a binary classification, in which 89% of the pixels cover land. This means that if our classification technique picked up no water at all, then 89% of our pixels would be observed correctly.

This point is highlighted in Fig. 11, in which we see the spatial distribution of classification errors for the month of August 2011 over the Aral Sea, when using σ^0_{30} or SDR in the classification process. White regions show where both methods are correct. In both cases, this includes the majority of the area of the true lake extents. Blue regions show where the SDR method alone is incorrect. These are confined mainly to the region of inflow from Uzbekistan via the Amu Darya river, and some of this error may be attributed to the relative timing of the snapshot MODIS reference image used in the kappa test, when compared with the wider temporal range of acquisition of GM data used in the SDR method. The grey regions are where only the σ^0_{30} classification method produces incorrect results. Most of this represents land incorrectly classified as water. The considerable extent of these misclassified pixels in comparison to the size of the actual lakes is the reason for the corresponding kappa statistic of 0.25. The pixels in red were misclassified using both σ^0_{30} and SDR methods. Discrepancies at the boundaries between land and water are to be expected. Firstly they form a continuous region of values close to the thresholds of the variable used in the classification as well as the MODIS reflectance used for the reference map. Secondly, where water represents a certain fraction of a pixel at the land–water boundary, the coherent summation of the radar signals may produce a different response to that of the SWIR MODIS signal, in terms of which side of the threshold the value finally falls.

3.7. Aral Sea time series of spatial extents

The resulting maps of the spatial extents of the Aral Sea through the non-frozen months of 2011 are shown overlain consecutively onto a terrain relief map in Fig. 12. It must be remembered at this point that the extents captured represent 100% water fraction—that is, total inundation of each pixel. This arises from the method chosen. We were using MODIS SWIR values as a baseline by which to validate our classification methods. Determining the precise boundary between water and land using MODIS and the within-pixel water fraction is itself complex (e.g. Li, Sun, Yu, et al. (2013), Li, Sun, Goldberg, and Stefanidis (2013)), which led us to use a reflectance threshold at a level that excluded boundary values, as discussed in the Method section above.

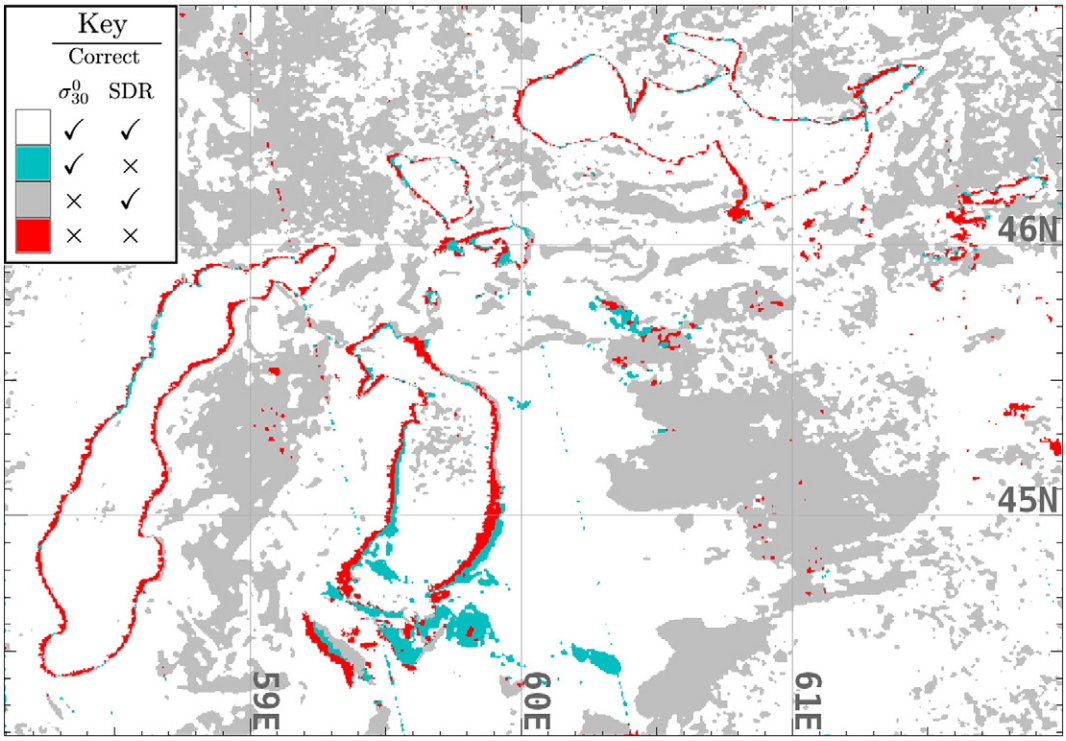

Fig. 11. Classification errors in σ^0_{30} and SDR water maps for the month of August 2011. 69% of pixels in the σ^0_{30} classification are correct. However, as can be seen by the grey areas above, the spatial distribution of correct pixels would lead to a very poor result, which is reflected in the kappa value of 0.25. Similarly, 97% of pixels in the SDR classification are correct, but as the proportion of incorrect water pixels (shown in blue and red) with respect to their total is more significant, the kappa value only reaches 0.83.

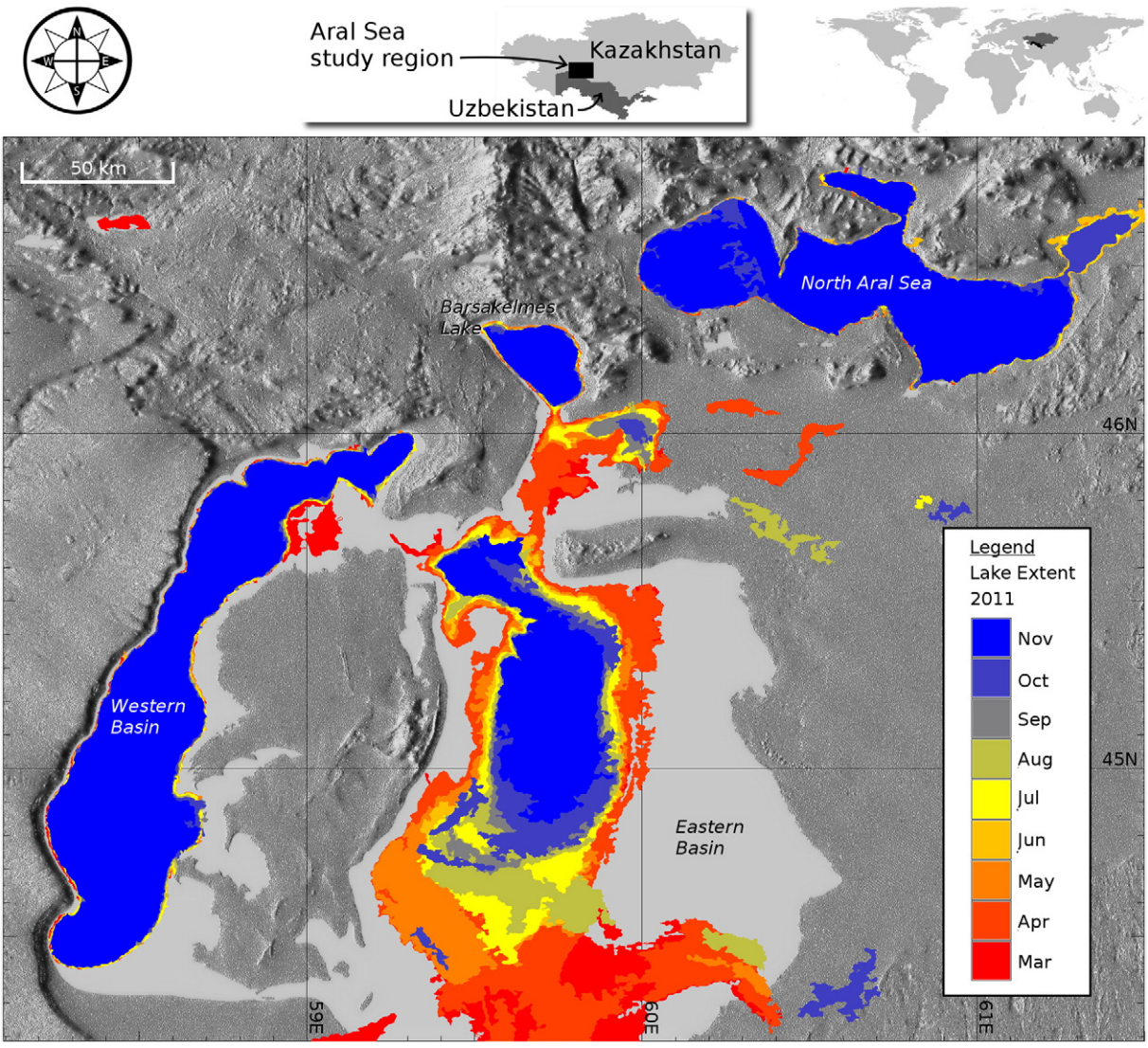

Fig. 12. Monthly spatial extents of the Aral Sea between March and November 2011, as determined using the SDR method.

4. Conclusion

Access to high temporal frequency ScanSAR data acquired from multiple incidence angles provides a means to increase the accuracy by which we can segregate open water using radar data. Using these methods, spatial accuracy and certainty may be increased at the expense of temporal precision. For the arid environment dominating our study region, SDR provided the most accurate means of classification, and both SDR and β were far more stable and accurate classifiers than backscatter alone. It is reasonable to suppose that different surface conditions may reverse the relative accuracy of SDR and β, but this remains to be tested.

Current readily-available satellite C-band capabilities rest with the Canadian Space Agency's Radarsat-2 mission, but ESA's next SAR-enabled satellite constellation, Sentinel-1, is due to commence this year with the planned launch of Sentinel-1A, with 1B scheduled for 2015. It is intended that the constellation, in its scanSAR modes, be capable of daily coverage north of 45° and south of −45° (Fletcher, 2012). Capabilities will increase as new units are added to the constellation, up to the target maximum of six. Meanwhile, the Canadian Space Agency (CSA) is planning to launch the Radarsat Constellation in 2018, which is forecast to provide "daily access to 95% of the world" (CSA, 2013). In light of the fact that both systems are being developed under the framework of mutual interoperability agreements (Fletcher, 2012), it is not too optimistic to assume the potential for global daily C-band radar coverage, at a resolution of at least 500 m (and possibly as little as 100 m) by the end of the decade.

As the weekly coverage of C-band data increases from 7 to 10 instances and beyond, we can conclude from the work done here that our ability to produce accurate global flood maps, independent of cloud cover and with little interference from wind-induced roughening effects, will be greatly increased for open water in arid regions. When coupled with the predicted water surface elevation measurement capabilities of the Surface Water and Ocean Topography (SWOT) mission, due for launch in 2019 (CNES, 2013; Durand et al., 2010), our ability to monitor global surface water volumes, discharges and dynamics will be greatly enhanced. However, this will be limited by the remaining challenges to increasing the accuracy of classification of smaller water bodies, particularly where pixels are mixed at boundaries and regions of partial inundation.

References

Aires, F., Papa, F., & Prigent, C. (2013). A long-term, high-resolution wetland dataset over the Amazon basin, downscaled from a multiwavelength retrieval using SAR data. *Journal of Hydrometeorology*, *14*(2), 594–607.

Arnesen, A. S., Silva, T. S., Hess, L. L., Novo, E. M., Rudorff, C. M., Chapman, B.D., et al. (2013). Monitoring flood extent in the lower Amazon river floodplain using ALOS/PALSAR ScanSAR images. *Remote Sensing of Environment*, *130*, 51–61.

Ban, Y., Hu, H., & Rangel, I. M. (2010). Fusion of Quickbird MS and RADARSAT SAR data for urban land-cover mapping: Object-based and knowledge-based approach. *International Journal of Remote Sensing*, *31*(6), 1391–1410.

Bartsch, A., Wagner, W., Scipal, K., Pathe, C., Sabel, D., & Wolski, P. (2009). Global monitoring of wetlands — The value of ENVISAT ASAR global mode. *Journal of Environmental Management*, *90*(7), 2226–2233.

Bass, A.M., O'Grady, D., Berkin, C., Leblanc, M., Tweed, S., Nelson, P. N., et al. (2013). High diurnal variation in dissolved inorganic C, $\delta^{13}C$ values and surface efflux of CO_2 in a seasonal tropical floodplain. *Environmental Chemistry Letters*, 1–7. http://dx.doi.org/10.1007/s10311-013-0421-7.

Baup, F., Mougin, E., Hiernaux, P., Lopes, A., De Rosnay, P., & Chenerie, I. (2007). Radar signatures of Sahelian surfaces in Mali using ENVISAT-ASAR data. *IEEE Transactions on Geoscience and Remote Sensing*, *45*(7), 2354–2363.

Breckle, S. -W., Wucherer, W., & Dimeyeva, L. (2012a). Aralkum — A man-made desert. *Vegetation of the Aralkum*, *218*(8), 127–159 (Ch.).

Breckle, S. W., Wucherer, W., Dimeyeva, L. A., & Ogar, N.P. (Eds.). (2012). *Aralkum — A man-made desert. Vol. 218 of Ecological Studies*. Berlin, Heidelberg Springer.

Bwangoy, J. -R. B., Hansen, M. C., Roy, D. P., Grandi, G. D., & Justice, C. O. (2010). Wetland mapping in the Congo basin using optical and radar remotely sensed data and derived topographical indices. *Remote Sensing of Environment*, *114*(1), 73–86.

CNES (2013). *SWOT: A French-American mission to monitor the world's oceans and continental surface waters.* Website. Centre National d'Études Spatiales (http://smsc.cnes.fr/SWOT/, last viewed online 5-Jun-2013)

CSA (2013). RADARSAT constellation. Canadian Space Agency (http://www.asc-csa.gc.ca/eng/satellites/radarsat/default.asp, last viewed online 3-Jun-13)

Dronova, I., Gong, P., & Wang, L. (2011). Object-based analysis and change detection of major wetland cover types and their classification uncertainty during the low water period at Poyang lake, China. *Remote Sensing of Environment*, *115*(12), 3220–3236.

Durand, M., Fu, L., Lettenmaier, D., Alsdorf, D., Rodriguez, E., & Esteban-Fernandez, D. (2010). The surface water and ocean topography mission: Observing terrestrial surface water and oceanic submesoscale eddies. *Proceedings of the IEEE*, *98*, 766–779.

ESA (2009). ESA data products: Envisat ASAR. *Earthnet Online*. European Space Agency (http://earth.esa.int/object/index.cfm?fobjectid=1536, viewed online 15-May-2013)

Fletcher, K. (Ed.). (March 2012). *Sentinel-1: ESA's Radar Observatory Mission for GMES Operational Services, ESA sp-1322/1 Edition*. ESTEC, PO Box 299, 2200 AG Noordwijk, The Netherlands ESA Communications.

Frappart, F., Seyler, F., Martinez, J. -M., León, J. G., & Cazenave, A. (2005). Floodplain water storage in the negro river basin estimated from microwave remote sensing of inundation area and water levels. *Remote Sensing of Environment*, *99*(4), 387–399.

Gan, T., Zunic, F., Kuo, C., & Strobl, T. (2012). Flood mapping of Danube river at Romania using single and multi-date ERS2-SAR images. *International Journal of Applied Earth Observation and Geoinformation*, *18*, 68–81.

Gray, J., & Song, C. (2013). Consistent classification of image time series with automatic adaptive signature generalization. *Remote Sensing of Environment*, *134*, 333–341.

Grings, F., Salvia, M., Karszenbaum, H., Ferrazzoli, P., Kandus, P., & Perna, P. (2009). Exploring the capacity of radar remote sensing to estimate wetland marshes water storage. *Journal of Environmental Management*, *90*(7), 2189–2198.

Haas, E. M., Bartholomé, E., Lambin, E. F., & Vanacker, V. (2011). Remotely sensed surface water extent as an indicator of short-term changes in ecohydrological processes in sub-Saharan Western Africa. *Remote Sensing of Environment*, *115*(12), 3436–3445.

Henderson, F. M., & Lewis, A. J. (2008). Radar detection of wetland ecosystems: A review. *International Journal of Remote Sensing*, *29*(20), 5809–5835.

Hess, L. L., & Melack, J. M. (2003). Remote sensing of vegetation and flooding on Magela Creek Floodplain (Northern Territory, Australia) with the SIR-C synthetic aperture radar. *Hydrobiologia*, *500*(1–3), 65–82.

Hess, L., Melack, J., Filoso, S., & Wang, Y. (1995). Delineation of inundated area and vegetation along the Amazon floodplain with the SIR-C synthetic aperture radar. *IEEE Transactions on Geoscience and Remote Sensing*, *33*(4), 896–904.

Hostache, R., Matgen, P., Schumann, G., Puech, C., Hoffmann, L., & Pfister, L. (2009). Water level estimation and reduction of hydraulic model calibration uncertainties using satellite SAR images of floods. *IEEE Transactions on Geoscience and Remote Sensing*, *47*(2), 431–441.

Hudson, W. D., & Ramm, C. W. (1987). Correct formulation of the Kappa-coefficient of agreement. *Photogrammetric Engineering and Remote Sensing*, *53*(4), 421–422.

Jarvis, A., Reuter, H., Nelson, A., & Guevara, E. (2008). *Hole-filled SRTM for the globe version 4, available from the CGIAR-CSI SRTM 90 m database.* Website. Consortium for Spatial Information (http:/srtm.csi.cgiar.org, last viewed online 12-Apr-13)

Kellndorfer, J. M., Pierce, L. E., Dobson, M. C., Member, S., & Ulaby, F. T. (1998). Toward consistent regional-to-global-scale vegetation characterization using orbital SAR systems. *IEEE Transactions on Geoscience and Remote Sensing*, *36*(5), 1396–1411.

Lang, M., Townsend, P., & Kasischke, E. (2008). Influence of incidence angle on detecting flooded forests using C-HH synthetic aperture radar data. *Remote Sensing of Environment*, *112*(10), 3898–3907.

Lasaponara, R. (2006). Estimating spectral separability of satellite derived parameters for burned areas mapping in the Calabria region by using SPOT-vegetation data. *Ecological Modelling*, *196*(1–2), 265–270.

Le Toan, T., Ribbes, F., Wang, L., Floury, N., Ding, K., Kong, J., et al. (1997). Rice crop mapping and monitoring using ERS-1 data based on experiment and modeling results. *IEEE Transactions on Geoscience and Remote Sensing*, *35*(1), 41–56.

Li, S., Sun, D., Goldberg, M., & Stefanidis, A. (2013a). Derivation of 30-m-resolution water maps from TERRA/MODIS and SRTM. *Remote Sensing of Environment*, *134*, 417–430.

Li, S., Sun, D., Yu, Y., Csiszar, I., Stefanidis, A., & Goldberg, M.D. (2013). A new short-wave infrared (SWIR) method for quantitative water fraction derivation and evaluation with EOS/MODIS and Landsat/TM data. *IEEE Transactions on Geoscience and Remote Sensing*, *51*(3), 1852–1862.

Liebe, J., van de Giesen, N., Andreini, M., Steenhuis, T., & Walter, M. (2009). Suitability and limitations of ENVISAT ASAR for monitoring small reservoirs in a semiarid area. *IEEE Transactions on Geoscience and Remote Sensing*, *47*(5), 1536–1547.

Marti-Cardona, B., Lopez-Martinez, C., Dolz-Ripolles, J., & Bladè-Castellet, E. (2010). ASAR polarimetric, multi-incidence angle and multitemporal characterization of Doñana wetlands for flood extent monitoring. *Remote Sensing of Environment*, *114*(11), 2802–2815.

Martinez, J., & Letoan, T. (2007). Mapping of flood dynamics and spatial distribution of vegetation in the Amazon floodplain using multitemporal SAR data. *Remote Sensing of Environment*, *108*(3), 209–223.

Mason, D., Davenport, I., Neal, J., Schumann, G. J. -P., & Bates, P. (2012). Near real-time flood detection in urban and rural areas using high-resolution synthetic aperture radar images. *IEEE Transactions on Geoscience and Remote Sensing*, *50*(8), 3041–3052.

Menges, C. H., Van Zyl, J. J., Hill, G. J. E., & Ahmad, W. (2001). A procedure for the correction of the effect of variation in incidence angle on AIRSAR data. *International Journal of Remote Sensing*, *22*(5), 829–841.

Mladenova, I., Lakshmi, V., Walker, J., Panciera, R., Wagner, W., & Doubkova, M. (2010). Validation of the ASAR global monitoring mode soil moisture product using the NAFE'05 data set. *IEEE Transactions on Geoscience and Remote Sensing*, *48*(6), 2498–2508.

NEST (2013). *Next @ESA SAR toolbox.* Website. European Space Agency (http://nest.array.ca/web/nest, last viewed online 12-Apr-13)

O'Grady, D., & Leblanc, M. (2013). Radar mapping of broad-scale inundation: Challenges and opportunities in Australia. *Stochastic Environmental Research and Risk Assessment*, 1–10. http://dx.doi.org/10.1007/s00477-013-0712-3.

O'Grady, D., Leblanc, M., & Gillieson, D. (2011). Use of ENVISAT ASAR global monitoring mode to complement optical data in the mapping of rapid broad-scale flooding in Pakistan. *Hydrology and Earth System Sciences*, *15*(11), 3475–3494.

O'Grady, D., Leblanc, M., & Gillieson, D. (2013). Relationship of local incidence angle with satellite radar backscatter for different surface conditions. *International Journal of Applied Earth Observation and Geoinformation*, *24*, 42–53.

Park, S. -E., Bartsch, A., Sabel, D., Wagner, W., Naeimi, V., & Yamaguchi, Y. (2011). Monitoring freeze/thaw cycles using ENVISAT ASAR global mode. *Remote Sensing of Environment*, *115*(12), 3457–3467.

Pathe, C., Wagner, W., Sabel, D., Doubkova, M., & Basara, J. (2009). Using ENVISAT ASAR global mode data for surface soil moisture retrieval over Oklahoma, USA. *IEEE Transactions on Geoscience and Remote Sensing*, *47*(2), 468–480.

Pontius, R. G., & Millones, M. (2011). Death to kappa: Birth of quantity disagreement and allocation disagreement for accuracy assessment. *International Journal of Remote Sensing*, *32*(15), 4407–4429.

Quegan, S., Le Toan, T., Yu, J., Ribbes, F., & Floury, N. (2000). Multitemporal ERS SAR analysis applied to forest mapping. *IEEE Transactions on Geoscience and Remote Sensing*, *38*(2), 741–753.

Ribbes, F. (1999). Rice field mapping and monitoring with RADARSAT data. *International Journal of Remote Sensing*, *20*(4), 745–765.

Rignot, E., Salas, W. A., & Skole, D. L. (1997). Mapping deforestation and secondary growth in Rondonia, Brazil, using imaging radar and thematic mapper data. *Remote Sensing of Environment*, *59*(2), 167–179.

Schumann, G., Di Baldassarre, G., & Bates, P. (2009). The utility of spaceborne radar to render flood inundation maps based on multialgorithm ensembles. *IEEE Transactions on Geoscience and Remote Sensing*, *47*(8), 2801–2807.

Small, D., & Schubert, A. (2008). *Guide to ASAR geocoding. RSL-ASAR-GC-AD (1.0).*

Smith, A.M. S., Drake, N. A., Wooster, M. J., Hudak, A. T., Holden, Z. A., & Gibbons, C. J. (2007). Production of landsat etm + reference imagery of burned areas within southern African savannahs: Comparison of methods and application to MODIS. *International Journal of Remote Sensing*, *28*(12), 2753–2775.

Töyrä, J., & Pietroniro, A. (2005). Towards operational monitoring of a northern wetland using geomatics-based techniques. *Remote Sensing of Environment*, *97*, 174–191.

Töyrä, J., Pietroniro, A., & Martz, L. W. (2001). Multisensor hydrologic assessment of a freshwater wetland. *Remote Sensing of Environment*, *75*, 162–173 (July 2000).

USGS (2013). *Global visualization viewer.* Website. US Geological Survey Earth Resources Observation and Science Center (http://glovis.usgs.gov, last viewed online 21-May-2013)

Veraverbeke, S., Harris, S., & Hook, S. (2011). Evaluating spectral indices for burned area discrimination using MODIS/ASTER (MASTER) airborne simulator data. *Remote Sensing of Environment*, *115*(10), 2702–2709.

Zink, M., Buck, C., Suchail, J. -L., Torres, R., Bellini, A., Closa, J., et al. (2001). *The radar imaging instrument and its applications: ASAR. ESA Bulletin*, *106*, European Space Agency.